

MUTE-SLAM: Real-Time Neural SLAM with Multiple Tri-Plane Hash Representations

Yifan Yan¹, Ruomin He¹, and Liu Zhenghua¹

Beihang University, China

Abstract. We introduce MUTE-SLAM, a real-time neural RGB-D SLAM system employing multiple tri-plane hash-encodings for efficient scene representation. MUTE-SLAM effectively tracks camera positions and incrementally builds a scalable multi-map representation for both small and large indoor environments. It dynamically allocates sub-maps for newly observed local regions, enabling constraint-free mapping without prior scene information. Unlike traditional grid-based methods, we use three orthogonal axis-aligned planes for hash-encoding scene properties, significantly reducing hash collisions and the number of trainable parameters. This hybrid approach not only ensures real-time performance but also enhances the fidelity of surface reconstruction. Furthermore, our optimization strategy concurrently optimizes all sub-maps intersecting with the current camera frustum, ensuring global consistency. Extensive testing on both real-world and synthetic datasets has shown that MUTE-SLAM delivers state-of-the-art surface reconstruction quality and competitive tracking performance across diverse indoor settings. The code will be made public upon acceptance of the paper.

Keywords: Tri-plane Hash-Encoding · Multi-Map Representation · Scalability

1 Introduction

Dense Simultaneous Localization and Mapping (SLAM) has been a fundamental challenge in 3D computer vision for decades, playing a crucial role in applications like robotics, virtual/augmented reality, and autonomous driving. A robust dense SLAM system equipped with RGB-D sensors needs to track camera poses effectively while reconstructing the environment into a high-fidelity map.

Traditional dense SLAM methods [7, 9, 18–20, 22, 27, 32, 34] generate accurate localization results and detailed 3D point positions, but they fall short in rendering novel views or filling unobserved regions. Learning-based systems [5, 10, 26] have shown promise in large-scale scenes and global 3D map production, yet their reconstruction performance is limited and requires retraining for different scenarios.

With the advent of Neural Radiance Field (NeRF) [16], efforts have been made to integrate it into SLAM systems due to its capability to render novel views [2–4, 31] and reconstruct 3D surfaces [1, 14, 21, 30]. NeRF-based SLAM

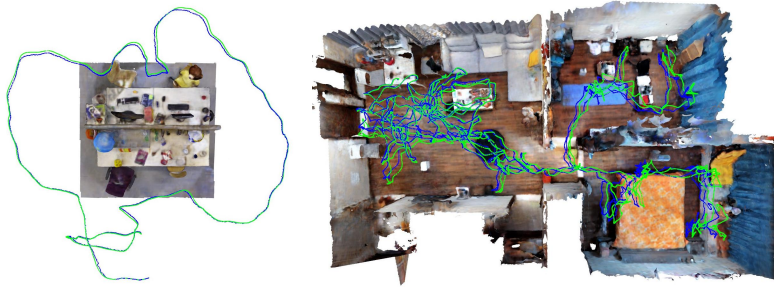


Fig. 1: Our MUTE-SLAM system demonstrates rapid and accurate tracking and mapping across indoor environments of varying scales without pre-defined boundaries. We depict the trajectories and meshes of both a small and a large scenario: estimated trajectories are marked in blue, while ground truths are in green. The left image is an around-a-desk scene from the TUM-RGBD dataset [24], while the image on the right is a multiple-room scene from Apartment dataset provided by NICE-SLAM [35].

methods iMAP [25] and NICE-SLAM [35], have demonstrated their applicability across various scenes and ability to predict the appearance of unobserved areas, although their computational demands hinder real-time application. Recent works [11, 28] utilize hash-encoded voxel grids [17] to accelerate convergence and enhance detail fidelity. Despite hash collisions can be implicitly mitigated by the original design of Instant-NGP [17], the reconstructed mesh still suffers from aliasing. As proved in [12, 13, 15, 15, 36], projecting spatial points into a tri-plane representation can efficiently reduce scene parameters while preserving geometric and color information. Therefore following [13], we leverage a tri-plane hash-encoding method to store scene features and minimize hash collisions. Moreover, current Nerf-based SLAM systems [12, 25, 28, 35] require pre-set scene boundaries, limiting their application in unknown environments. Some [11, 33] address this with octree-based voxel grids, but they still necessitate an initially defined loose boundary and struggle to reconstruct beyond these limits. Our proposed MUTE-SLAM overcomes this by introducing a multi-map-based scene representation. Through dynamically allocating new sub-maps upon detecting new areas, MUTE-SLAM can be deployed in environments of any size given reasonable RGB-D sensor observations.

In summary, our contributions include:

- A multi-map-based scene representation facilitating reconstruction scalable to diverse indoor scenarios.
- A tri-plane hash-encoding method for sub-maps which enables real-time tracking and anti-aliasing dense mapping with high-fidelity details.
- A optimization strategy that jointly optimizes all sub-maps observed currently, ensuring global consistency.
- Extensive experimental validation on various datasets, demonstrating our system’s scalability and effectiveness in both tracking and mapping.

2 Related Works

2.1 Dense Visual SLAM

DTAM [19] is the first dense SLAM system to employ direct methods, utilizing information from all pixels for tracking by comparing newly inputted RGB frames with a reconstructed dense model. KinectFusion [18], leveraging a RGB-D sensor, uses a volumetric Truncated Signed Distance Function (TSDF) to fuse scene geometry and tracks camera positions via Iterative Closest Point (ICP). Subsequent works have focused on improving scalability through new data structures [20,34], enhancing global consistency with Bundle Adjustment (BA) [7,22], and increasing efficiency [32]. Recent learning-based methods [5, 10, 26] demonstrate superior accuracy and robustness compared to traditional approaches on single scenes, but they struggle with generalization across varied scenes.

2.2 Neural Implicit SLAM

iMAP [25] is the first SLAM system to incorporate NeRF [16], it models the environment into a single Multilayer Perceptron (MLP) and jointly optimizes the map and camera poses. NICE-SLAM [35] substitutes the scene representation in iMAP with hierarchical voxel grids to resolve the forgetting issue, achieving enhanced tracking and mapping in large indoor environments. However, both approaches face limitations in handling unknown environments due to the requirement for a prior scene boundary. Vox-Fusion [33] attempts to address this by introducing octree-based voxel grids as the map representation but is still limited to the initially defined spatial scope.

Recent advancements in NeRF-based SLAM have improved tracking, mapping, and running speed. ESLAM [12] stores features on multi-scale axis-aligned planes and employs rendering based on TSDF. Co-SLAM [28] combines coordinate and hash-encodings for input points to achieve both smooth meshes and fast convergence, and introduces a real-time global bundle adjustment mechanism using a ray list sampled from past keyframes. Despite these improvements, scalability remains a challenge. Our work addresses this by introducing a multi-map solution with an accompanying optimization strategy. Besides, we represent each sub-map with a tri-plane hash-encoding which allows for fast convergence and detailed surface reconstruction. Concurrent work [8] also adopts a tri-plane multi-map representation, but differs from ours in using a joint coordinate and tri-plane encoding, as well as in local map allocation and optimization strategies.

3 Method

The overview of MUTE-SLAM is illustrated in Fig. 2. Given an input RGB-D stream $\{I_i, D_i\}_{i=1}^M$, the system tracks their 6-DOF camera poses $\{T_i : R_i | t_i\}_{i=1}^M$ and conducts mapping to optimize a multi-map implicit scene representation $\{E_k\}_{k=1}^S$. When the camera captures a new region, a corresponding sub-map is

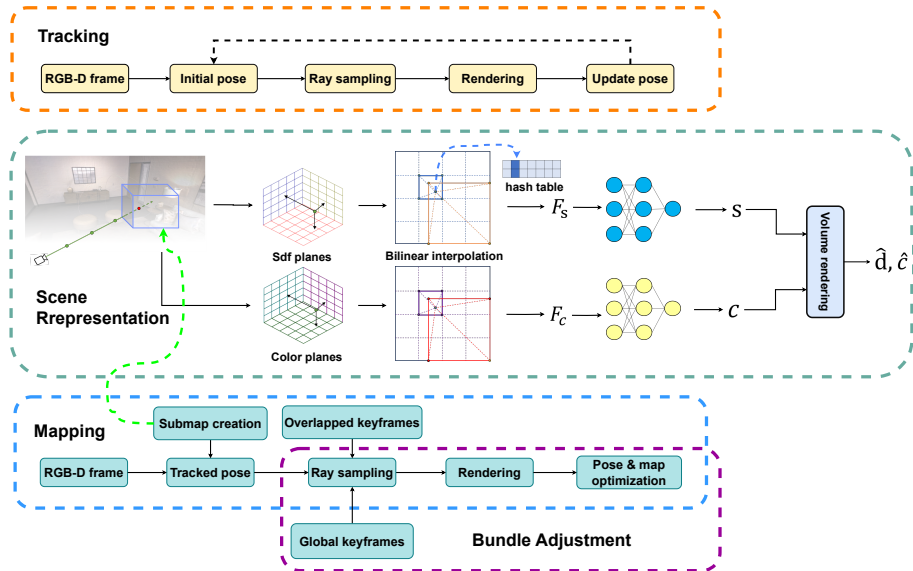


Fig. 2: The overview of MUTE-SLAM. Our method consists of three parts. 1) Scene representation: the whole scene is represented by several sub-maps created on the fly. Each sub-map is formulated by double tri-plane hash-encoders, one for TSDF and the other for color encoding. 2) Tracking: this module optimizes the pose for each frame through differentiable rendering. 3) Mapping: the mapping module dynamically allocates new sub-maps with a tracked pose. It conducts a joint optimization of both scene and pose parameters, utilizing the current frame along with co-visible keyframes. 4) Bundle Adjustment: by sampling keyframes globally, this module further refines all trainable parameters and ensures global consistency.

created to represent it, as detailed in Sec. 3.1. Each local map E_k encodes a point coordinate \mathbf{p} within its domain with three orthogonal TSDF feature planes and three color planes, as described in Sec. 3.2. These features from the sub-maps are decoded into TSDF and color using two separate MLPs, initiating the volume rendering process (Sec. 3.3). The rendered depth and color images are subsequently utilized to jointly optimize the sub-maps and camera poses. Additionally, periodic global bundle adjustments are implemented to ensure global consistency (Sec. 3.4).

3.1 Multi-map Scene Representation

As previous neural implicit SLAM methods [12, 25, 28, 33, 35] are restricted to functioning within pre-defined scene boundaries, they are unsuitable for navigating and mapping large, unknown indoor environments. Consequently, performing tracking and mapping incrementally with no prior environment information becomes a critical issue. MUTE-SLAM addresses this problem by adopting a multi-map scene representation approach. We encode the whole scene with sev-

eral sub-maps $\{E_k\}_{k=1}^S$, each to express a local region, enabling the reconstruction of indoor scenes of arbitrary shapes and sizes.

After tracking an input RGB-D frame, points are randomly sampled from the depth image and projected into the world coordinate system with the estimated camera pose $\{T_i : R_i | t_i\}$. Points with invalid depths are filtered out, and outliers are removed to mitigate noise. If the proportion of points that fall outside all existing sub-maps exceeds a predetermined threshold P , a new local map E_k is generated. The local map’s size is determined by extending the cuboid vicinity of the current camera position and the points that are out of bounds over a length of l , which is a hyperparameter. The redundancy of a sub-map’s boundary would reduce the number of total sub-maps, thereby lowering memory consumption. Concurrently, the corresponding frame is added to the global keyframe database. For optimization, rays are sampled from the current frame and co-visible keyframes. Rays terminating outside all sub-maps are removed from the training process. Specifically, rather than optimizing a single sub-map at a time, we simultaneously optimize all observed sub-maps to ensure global consistency as a input frame’s frustum may intersect with multiple sub-maps. Global bundle adjustments are also employed periodically to further enhance global consistency.

3.2 Tri-plane Hash Encoding

Lately, hash-encoding [17] has gained much attention in the NeRF community [4, 11, 14, 28] due to its fast convergence and strong environmental representation capabilities. Despite that, hash collisions are inevitable and could lead to artifacts in the reconstructed scenes. The standard solution is to let the light MLP decoder handle hash collisions implicitly or use larger hash tables. But as the scene grows large and complicated, the MLP will reach its limit and a capacious hash table consumes substantial memory space. Meanwhile, tri-plane encoding approaches [12, 13, 15, 15, 36] have demonstrated competence in surface and appearance reconstruction with low memory consumption. Combining the advantages of both worlds, we represent each sub-map by tri-plane hash-encoding.

In MUTE-SLAM, a local map E_k is encoded by three orthogonal planes for TSDF $\{E_{xy}^s, E_{xz}^s, E_{yz}^s\}$ and another three for color $\{E_{xy}^c, E_{xz}^c, E_{yz}^c\}$, each plane denotes a 2D hash encoder as in [17]. All planes share the same resolution levels L , base resolution N_{min} , finest resolution N_{max} , per level feature dimension χ and hash table size H . The finest resolution N_{max} and hash table size H are determined by the local map volume $V[m^3]$:

$$N_{max} = \lfloor 50 \cdot V^{\frac{1}{3}} \rfloor \quad (1)$$

$$H = N_{max}^2 \quad (2)$$

Other parameters are set as hyperparameters. When a point falls within a sub-map, it is orthogonally projected onto the corresponding planes. The encoder

then interpolates the point features bilinearly by querying the nearest four vertices from each level of the hash table, concatenating features across all levels to produce the final output. Consequently, the TSDF and color feature vectors $\{F_s, F_c\}$ are derived by summing up the outputs from the three planes:

$$F_s(\mathbf{p}) = E_{xy}^s(\mathbf{p}) + E_{xz}^s(\mathbf{p}) + E_{yz}^s(\mathbf{p}) \quad (3)$$

$$F_c(\mathbf{p}) = E_{xy}^c(\mathbf{p}) + E_{xz}^c(\mathbf{p}) + E_{yz}^c(\mathbf{p}) \quad (4)$$

We employ two separate double-layer MLPs $\{f_s, f_c\}$ to decode the TSDF and RGB values respectively:

$$s(\mathbf{p}) = f_s(F_s(\mathbf{p})) \quad (5)$$

$$\mathbf{c}(\mathbf{p}) = f_c(F_c(\mathbf{p})) \quad (6)$$

The TSDF and color values are then utilized in the volume rendering module. The plane-based representation, growing quadratically with scene size, results in fewer hash table queries and hence fewer collisions compared to grid representations, given equal hash table sizes. Furthermore, since a point’s feature vector is a composite of inputs from three distinct encoders, the probability of encountering conflicts across all encoders is significantly reduced. In situations where collisions do occur in one encoder, the impact is mitigated by the inputs from the other encoders, thus lessening the overall adverse effect. Sec. 4.4 demonstrates the effectiveness of our tri-plane hash-encoding.

3.3 TSDF-based Volume Rendering

MUTE-SLAM follows the TSDF-based rendering procedure in [12]. For an input frame i , we sample randomly from pixels with valid depths, casting rays into the world coordinate system using the estimated pose $\{T_i : R_i | t_i\}$. We apply stratified sampling to acquire $N = N_g + N_d$ points along a ray, distributed between the *near* and *far* bounds. Initially, N_g points are uniformly sampled across the entire sampling region. Then within a smaller truncated distance $[d - \delta, d + \delta]$ near the surface, extra N_d points are sampled uniformly, where d denotes the ground truth depth value.

Each sampled point $\mathbf{p}_n = \mathbf{o} + d_n \mathbf{r}$ is represented by the ray’s origin \mathbf{o} , direction \mathbf{r} and depth d_n . For all points $\{\mathbf{p}_n\}_{n=1}^N$ along a ray, we predict the color $\hat{\mathbf{c}}$ and depth \hat{d} with color and TSDF values $\{\mathbf{c}(\mathbf{p}_n), s(\mathbf{p}_n)\}$ retrieved from MLPs:

$$\hat{\mathbf{c}} = \sum_{n=1}^N \omega_n \mathbf{c}(\mathbf{p}_n), \quad \hat{d} = \sum_{n=1}^N \omega_n d_n \quad (7)$$

For ω_n , as in [21], it is derived from the volume density $\sigma(\mathbf{p}_n)$ and TSDF value $s(\mathbf{p}_n)$:

$$\sigma(\mathbf{p}_n) = \beta \cdot \text{Sigmoid}(-\beta \cdot s(\mathbf{p}_n)) \quad (8)$$

$$\omega_n = \exp\left(-\sum_{k=1}^{n-1} \sigma(\mathbf{p}_k)\right) \cdot [1 - \exp(-\sigma(\mathbf{p}_n))] \quad (9)$$

Here, β is a learnable parameter which controls the sharpness of surfaces.

3.4 Tracking and Mapping

Loss Functions. We apply four loss functions to optimize the scene representation, MLPs and camera poses: RGB loss, depth loss, TSDF loss and free-space loss. Once a batch of rays R are selected, the RGB and depth loss are obtained as l_2 errors between rendered and ground truth values:

$$L_{rgb} = \frac{1}{|R|} \sum_{r \in R} (\hat{\mathbf{c}}(\mathbf{r}) - \mathbf{c}(\mathbf{r}))^2 \quad (10)$$

$$L_{depth} = \frac{1}{|R|} \sum_{r \in R} (\hat{d}(\mathbf{r}) - d(\mathbf{r}))^2 \quad (11)$$

The free-space loss is applied to supervise the points far from the surfaces ($|d_p - d(r)| > \delta$) to have a truncated TSDF value of 1:

$$L_{fs} = \frac{1}{|R|} \sum_{r \in R} \frac{1}{|N_{fs}|} \sum_{\mathbf{p} \in N_{fs}} (s(\mathbf{p}) - 1)^2 \quad (12)$$

For points near the surface ($|d_p - d(r)| \leq \delta$), similar to [12], we further split them into two parts to obtain the TSDF loss:

$$L_{mid} = \frac{1}{|R|} \sum_{r \in R} \left[\frac{\lambda_{mid}}{|N_{mid}|} \sum_{\mathbf{p} \in N_{mid}} (s(\mathbf{p}) + d(r) - d_p)^2 \right] \quad (13)$$

$$L_{tail} = \frac{1}{|R|} \sum_{r \in R} \left[\frac{\lambda_{tail}}{|N_{tail}|} \sum_{\mathbf{p} \in N_{tail}} (s(\mathbf{p}) + d(r) - d_p)^2 \right] \quad (14)$$

$$L_{tsdf} = L_{mid} + L_{tail} \quad (15)$$

Where the middle points $\mathbf{p} \in N_{mid}$ with depths reside in $[d(r) - 0.4\delta, d(r) + 0.4\delta]$ have a larger weight λ_{mid} , while the others have a smaller weight λ_{tail} . The final loss is the weighted sum of the objective functions above:

$$L_{all} = \lambda_{rgb} \cdot L_{rgb} + \lambda_{depth} \cdot L_{depth} + \lambda_{fs} \cdot L_{fs} + L_{tsdf} \quad (16)$$

Tracking. We track the camera-to-world transformation matrix $T_i \in SE(3)$ for every input frame i . When receiving a input frame i , its initial pose is obtained using constant speed assumption:

$$T_i = T_{i-1} T_{i-2}^{-1} T_{i-1} \quad (17)$$

Then, the pose T_i is transformed into a seven-dimensional vector for optimization, which is formed by concatenating the rotation quaternion q_i and the translation vector t_i . We sample uniformly N_{cam} pixels from frame i and optimize the pose iteratively using all loss functions, while keeping the scene parameters and MLPs fixed.

Mapping. MUTE-SLAM performs mapping every K frames and inserts the mapped frame as a keyframe into the global keyframe database. When the mapping thread starts, we first sample N_{map} rays from the current frame and M keyframes having co-visibility with current frame. Then we filter out rays whose *far* bounds lay outside all sub-maps. Each point on the rays is encoded within the corresponding sub-map. Since we define loose boundaries for sub-maps, only the oldest map is used when points fall into the area where multiple sub-maps overlap. At last, we jointly optimize all observed sub-maps, MLPs and camera poses iteratively with the objective functions. Specifically, we use the ground truth pose at the first input frame and only optimize scene parameters and MLPs for initialization.

Bundle Adjustment. Once the keyframe database has accumulated a sufficient number of frames, global bundle adjustment is initiated for every twenty frames of input. From the keyframe database, G frames are globally sampled, with all trainable parameters optimized in a manner akin to the mapping thread. The global bundle adjustment module plays a crucial role in correcting drifting poses and bolstering global consistency.

4 Experiments.

4.1 Experimental Setup.

Baselines. We choose state-of-art NeRF-based dense SLAM approaches ESLAM [12] and Co-SLAM [28] as our main baselines for both surface reconstruction and camera tracking. To better evaluate our proposed MUTE-SLAM on pose estimation, we also compare with previous methods NICE-SLAM [35] and Vox-Fusion [33]. We run these methods using the default settings provided in their open-source code.

Datasets. We evaluate MUTE-SLAM on various 3D benchmarks of indoor scenarios. For quantitative evaluation of the reconstruction quality, we use 8 synthetic scenes from Replica [23]. To validate effectiveness on pose tracking, we conduct experiments on 6 real-world scenes from ScanNet [6] and 3 real-world scenes from TUM-RGBD [24] dataset. We also demonstrate the scalability of MUTE-SLAM on large-scale Apartment dataset provided by NICE-SLAM [35].

Metrics. For surface reconstruction, We adopt evaluation metrics *Depth L1* [cm], *Accuracy* [cm], *Completion* [cm] and *Completion ratio* [$< 5cm\%$]. Additionally, to underscore the ability of our method to produce detailed geometry compared to ESLAM [12], we incorporate the *Completion ratio* [$< 1cm\%$] metric. Following [1, 12, 29], before evaluation, we remove faces that are not inside any camera frustum or are occluded in all RGB-D frames from the reconstructed mesh. For the evaluation of camera tracking, we employ *ATE RMSE* [cm] [24].

Table 1: Quantitative results of reconstruction on Replica [23] dataset. The best results are bolded. Our proposed MUTE-SLAM outperforms Co-SLAM [28] and shows better or on-par performance compared to ESLAM [12].

Metrics	Method	Room0	Room1	Room2	Office0	Office1	Office2	Office3	Office4	Avg.
Depth L1 (cm) ↓	ESLAM	0.95	0.98	1.37	0.81	1.27	1.60	1.49	1.06	1.19
	Co-SLAM	1.47	1.44	3.70	1.99	1.71	7.76	5.42	2.73	3.22
	Ours	0.93	0.95	1.35	0.78	1.31	1.56	1.69	0.88	1.18
Acc. (cm) ↓	ESLAM	1.04	0.80	0.90	0.79	0.83	0.96	1.16	1.06	0.94
	Co-SLAM	1.04	0.91	1.01	0.88	0.70	1.86	1.94	1.12	1.18
	Ours	1.03	0.81	0.90	0.78	0.68	0.93	1.13	1.04	0.91
Comp. (cm) ↓	ESLAM	1.03	0.83	0.99	0.82	0.72	0.98	1.16	1.12	0.96
	Co-SLAM	1.06	0.93	1.21	0.93	0.77	1.34	1.46	1.26	1.12
	Ours	1.01	0.81	0.98	0.80	0.73	0.97	1.18	1.08	0.95
Comp. Ratio (%) ↑	ESLAM	99.71	99.70	99.08	99.46	99.40	99.35	98.98	98.87	99.31
	Co-SLAM	99.45	99.65	96.99	98.79	99.20	98.53	97.68	97.59	98.49
	Ours	99.77	99.79	99.22	99.51	99.38	99.22	98.84	99.04	99.34

Implementation Details. We run all experiments on a desktop PC with a 3.70GHz Intel i9-10900K CPU and an NVIDIA RTX 3080 GPU. For local map creation, the threshold P is set to 0.2 for Replica [23] and 0.25 for the other datasets, while the expanding size l is 1 m for Replica [23], 1.5 m for ScanNet [6], 2.5m for Apartment [35] and 3 m for TUM-RGBD [24]. Each hash encoder has the same base resolution $N_{min} = 16$, resolution levels $L = 16$, per level feature dimension $\chi = 2$, resulting in 32 dimensions of input for MLPs. The MLPs both have two hidden layers of 32 channels. For rendering, we set the near-surface truncated distance δ to 6 cm and regular sampling number N_g to 32. Particularly, we sample $N_d = 8$ near-surface points for Replica [23] and TUM-RGBD [24], and $N_d = 12$ points for ScanNet [6] and Apartment [35]. Please refer to the supplementary materials for further details of our implementation.

4.2 Evaluation of Mapping and Tracking

Evaluation on Replica [23]. We compare the reconstruction performance on Replica [23] only with Co-SLAM [28] and ESLAM [12] as they significantly outperform previous methods [25, 33, 35]. For quantitative analysis, we run each method five times and report the average results. As shown in Tab. 1, our approach outperforms Co-SLAM [28] on all scenes and shows competitive performance with ESLAM [12]. Due to the use of a joint coordinate and parametric encoding, Co-SLAM [28] tends to produce over-smoothed surfaces, which leads to the amplification of reconstruction error. Although ESLAM [12] achieves high overall accuracy, it falls short in preserving surface details. To further highlight our method’s superiority in capturing scene details, we compare the *Completion ratio* [$< 1cm\%$] with ESLAM [12] in Tab. 2. Qualitative results in Fig. 3 also demonstrate that MUTE-SLAM effectively reconstructs detailed environmental geometry with fewer artifacts.

Table 2: Comparison of *Completion ratio* [$< 1cm\%$] with ESLAM [12]. Our method demonstrates superior performance in all scenes, indicative of our approach’s ability to accurately preserve details and minimize artifacts in reconstructed scene structures.

Metrics	Method	Room0	Room1	Room2	Office0	Office1	Office2	Office3	Office4	Avg.
Comp. Ratio \uparrow	ESLAM	55.21	72.77	65.94	76.30	86.17	62.90	49.05	54.55	65.36
	Ours	56.29	74.55	66.62	76.93	88.61	64.28	49.51	55.67	66.56

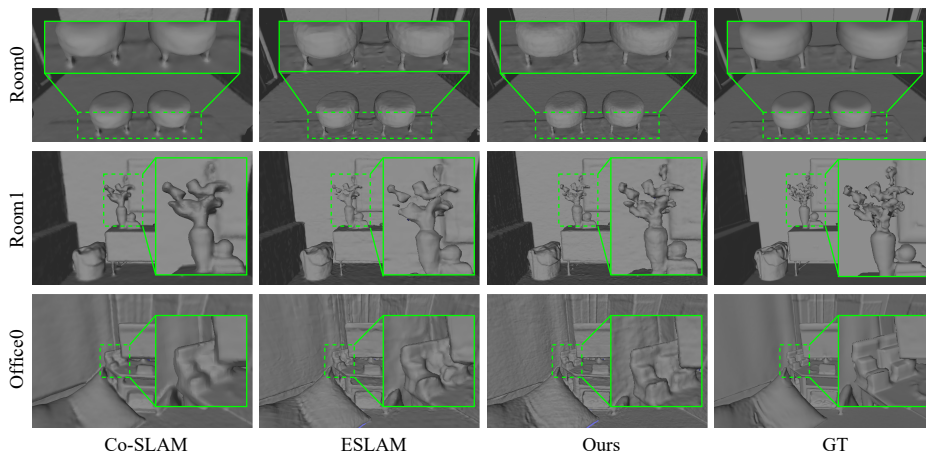


Fig. 3: Qualitative reconstruction results on Replica [23]. Our reconstructed mesh achieves a high level of completion and captures finer details of the environment, which are highlighted with green colored boxes across all methods.

Evaluation on ScanNet [6]. We assessed camera tracking accuracy on six real-world scenes from the ScanNet dataset [6] and report the average ATE RMSE [24] across five runs for each scene and method in Tab. 3. Our approach, MUTE-SLAM, exhibits competitive results in these tests. Notably, even without pre-defined scene boundaries, MUTE-SLAM consistently outperforms Co-SLAM [28] in all tested scenes. While ESLAM [12] achieves the best overall performance, it does so with twice the average processing time as ours (Tab. 6). Due to the incomplete nature of ScanNet [6] meshes, we present only qualitative reconstruction results in Fig. 4. These results highlight MUTE-SLAM’s ability to capture finer details and achieve a high level of completeness in reconstructions.

Evaluation on TUM RGB-D [24]. To further evaluate the tracking accuracy of MUTE-SLAM, we conducted experiments on real-world scenes from the TUM RGB-D dataset [24], with results averaged over five runs. Noted that ESLAM [12] runs unsuccessfully on the 'fr2/xyz' scene and has been consequently excluded from these comparative results. As shown in Tab. 4, our quantitative analysis reveals that MUTE-SLAM not only outperforms NICE-SLAM [35] and Co-SLAM [28] but also demonstrates competitive performance and superior ro-

Table 3: Quantitative results of ATE RMSE (cm) on ScanNet [6]. While ESLAM [12] yields the best overall performance, our method surpasses it in several scenes and secures the second-best overall result.

SceneID	0000	0059	0106	0169	0181	0207	Avg.
NICE-SLAM [35]	8.61	12.24	8.04	10.27	13.01	5.55	9.62
Vox-Fusion [33]	8.42	9.20	7.42	6.60	12.13	5.51	8.21
ESLAM [12]	7.37	8.31	7.59	6.45	9.29	5.65	7.44
Co-SLAM [28]	7.77	12.52	9.39	6.34	12.35	7.65	9.34
Ours	7.08	9.07	8.27	6.18	10.21	7.19	8.00

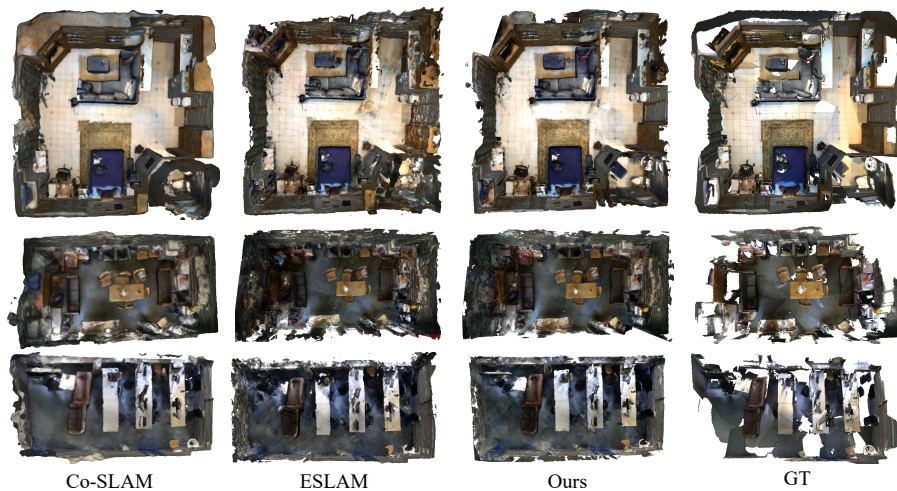


Fig. 4: Qualitative reconstruction results on ScanNet [6]. Our reconstructed mesh achieves better completion and fewer artifacts compared to ESLAM [12]. Additionally, our method produces sharper and more detailed geometry than Co-SLAM [28].

bustness compared to ESLAM [12], which takes hours to run on this dataset while ours only takes a few minutes.

Evaluation on Apartment [35] dataset. To demonstrate the effectiveness of our method in large scale indoor scenarios, we evaluate the tracking and surface reconstruction performance on Apartment dataset provided by NICE-SLAM [35]. As illustrated in Tab. 5, our method yields reasonable tracking performance. It should be emphasized that our method runs the fastest on this dataset, as discussed in Sec. 4.3.

4.3 Performance Analysis

We conducted a comparative analysis of the speed and memory consumption between our proposed MUTE-SLAM and the state-of-the-art methods ESLAM

Table 4: Quantitative results of ATE RMSE (cm) on TUM RGB-D [24] dataset. Instance of failure is denoted as N/A. Our proposed MUTE-SLAM outperforms NICE-SLAM [35] and Co-SLAM [28], while demonstrating competitive performance and superior robustness compared to ESLAM [12].

Method	fr1/desk(cm)	fr2/xyz(cm)	fr3/office(cm)
NICE-SLAM [35]	2.7	1.8	3.0
ESLAM [12]	2.5	N/A	2.8
Co-SLAM [28]	2.9	1.8	2.9
Ours	2.7	1.3	2.8

Table 5: Quantitative results of ATE RMSE (cm) on Apartment [35] dataset. The failed instance is denoted as N/A. Our approach generates reasonable tracking result on this dataset.

Method	NICE. [35]	Vox. [33]	ESLAM [12]	Co. [28]	Ours
ATE RMSE (cm) ↓	5.66	12.84	N/A	6.73	6.97

[12] and Co-SLAM [28]. Evaluations were performed on diverse scales of scenes: the small-scale 'room0' from Replica [23], the mid-scale '0000' from ScanNet [6], and the large-scale Apartment scene from NICE-SLAM [35]. Our metrics included average frame processing time (FPT) and the model's parameter count. As shown in Tab. 6, MUTE-SLAM not only operates faster in large scale scenes but also requires less memory compared to ESLAM [12]. Notably, in large-scale scenarios like Apartment [35], MUTE-SLAM achieves even speed advantages over Co-SLAM [28]. Moreover, the FPT and memory usage of MUTE-SLAM remain relatively stable across scene sizes, a benefit attributable to our scene representation design.

4.4 Ablations

Multi-map representation. We conducted ablation experiments on the Replica [23] and ScanNet [6] datasets to evaluate the impact of various components of our design. The quantitative results of this study are detailed in Tab. 7. Representing the scene with one map, our findings indicate that the multi-map representation improves tracking performance. This enhancement in tracking accuracy, in turn, leads to higher quality in the reconstruction process. This improvement can be attributed to our strategy for allocating submaps. By extending the boundaries of each submap over a defined length, the corresponding hash tables are able to attain larger sizes, which contributes to better overall system performance.

Tri-plane hash-encoding. To assess the effectiveness of tri-plane hash-encoding, we conducted an experiment where we replaced the tri-plane in each hash-encoding with a grid, while simultaneously tripling the maximum hash table size N_{max} . This adjustment marginally increases the overall capacity of the

Table 6: Run-time and memory comparison on Replica [23], ScanNet [6], and Apartment [35] scenes. ESLAM [12] and Co-SLAM [28] were evaluated using their default settings from the open-source code. MUTE-SLAM demonstrates faster performance in middle and large scale scenes compared to ESLAM [12], and shows a slight edge in speed over Co-SLAM [28] on the large scale Apartment scene [35]. MUTE-SLAM also maintains a reasonable speed in the small scale synthetic 'room0' scene from Replica [23].

	Method	Speed FPT(s)	# Param.
Replica [23]	ESLAM [12]	0.18	6.85M
	Co-SLAM [28]	0.12	0.26M
	Ours	0.21	6.28M
ScanNet [6]	ESLAM [12]	0.56	17.8M
	Co-SLAM [28]	0.19	1.59M
	Ours	0.28	10.73M
Apartment [35]	ESLAM [12]	2.40	22.1M
	Co-SLAM [28]	0.23	1.59M
	Ours	0.22	12.38M

Table 7: Quantitative results of ablation study. Our full model achieves the best tracking and overall mapping performance.

Method	Replica [23]				ScanNet [6]
	Acc.↓	Comp.↓	Comp. Ratio↑	Depth L1↓	ATE↓
w/o multi-map	1.04	1.00	99.34	1.20	9.64
w/o tri-plane	0.96	0.98	99.30	1.16	9.48
w/o global BA	1.06	1.08	99.17	1.27	12.06
ours full	1.03	1.01	99.74	0.93	8.00

hash tables compared to the tri-plane approach. Tab. 7 shows that tri-plane hash-encoding achieves superior tracking results, a higher completion ratio, and better-rendered depth images. Although grid hash-encoding excels in terms of accuracy and completion, it leads to artifacts in the reconstructed mesh due to hash collisions, which in turn affects tracking accuracy. As illustrated in Fig. 5, our qualitative comparison demonstrates that our proposed tri-plane hash-encoding effectively reduces aliasing and preserves scene details more accurately.

Global bundle adjustment. As illustrated in Tab. 7, the lack of global bundle adjustment leads to higher ATE errors and relatively low reconstruction performance. As global bundle adjustment corrects drifting poses and refines scene representation, it plays a critical role in ensuring robustness and global consistency in our method.

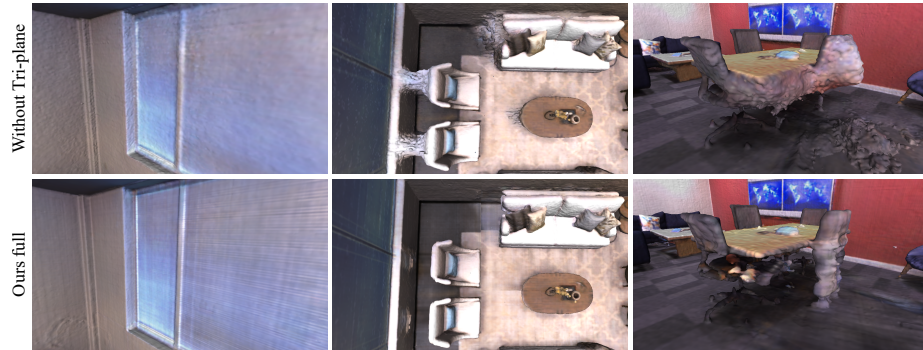


Fig. 5: Qualitative comparison of our method employing tri-plane hash-encoding versus without it, using reconstructed meshes from Replica [23] scenes. The left-most images illustrate how hash collisions can result in rough surfaces and low-quality textures in flat areas like walls and windows. Our tri-plane approach significantly mitigates these issues, achieving better results even with smaller hash tables. The other two images further show that our design leaves fewer artifacts in unobserved regions.

5 Conclusion

We presented MUTE-SLAM, a dense real-time neural RGB-D SLAM system utilizing multiple tri-plane hash-encodings as scene representation. We demonstrate that utilizing several sub-maps to express the scene ensures scalability, making our method applicable to various indoor scenarios. We also show that integrating tri-plane with hash-encoding diminishes hash collisions and trainable parameters, producing high-fidelity surface reconstruction and low memory usage. Moreover, we perform global bundle adjustment periodically to achieve accurate poses estimation and maintain global consistency.

Limitations. Our method relies on the valid observation of RGB-D sensors, thus is susceptible to illumination changes and inaccurate depth measurements. Additionally, our approach of randomly sampling from all historical keyframes for global bundle adjustment might result in insufficient optimization in less frequently observed regions, potentially compromising reconstruction quality in these areas.

References

1. Azinović, D., Martin-Brualla, R., Goldman, D.B., Nießner, M., Thies, J.: Neural rgb-d surface reconstruction. In: Proceedings of the IEEE/CVF Conference on Computer Vision and Pattern Recognition. pp. 6290–6301 (2022) **1, 8**
2. Barron, J.T., Mildenhall, B., Tancik, M., Hedman, P., Martin-Brualla, R., Srinivasan, P.P.: Mip-nerf: A multiscale representation for anti-aliasing neural radiance fields. In: Proceedings of the IEEE/CVF International Conference on Computer Vision. pp. 5855–5864 (2021) **1**

3. Barron, J.T., Mildenhall, B., Verbin, D., Srinivasan, P.P., Hedman, P.: Mip-nerf 360: Unbounded anti-aliased neural radiance fields. In: Proceedings of the IEEE/CVF Conference on Computer Vision and Pattern Recognition. pp. 5470–5479 (2022) [1](#)
4. Barron, J.T., Mildenhall, B., Verbin, D., Srinivasan, P.P., Hedman, P.: Zip-nerf: Anti-aliased grid-based neural radiance fields. arXiv preprint arXiv:2304.06706 (2023) [1](#), [5](#)
5. Bloesch, M., Czarnowski, J., Clark, R., Leutenegger, S., Davison, A.J.: Codeslam—learning a compact, optimisable representation for dense visual slam. In: Proceedings of the IEEE conference on computer vision and pattern recognition. pp. 2560–2568 (2018) [1](#), [3](#)
6. Dai, A., Chang, A.X., Savva, M., Halber, M., Funkhouser, T., Nießner, M.: Scannet: Richly-annotated 3d reconstructions of indoor scenes. In: Proceedings of the IEEE conference on computer vision and pattern recognition. pp. 5828–5839 (2017) [8](#), [9](#), [10](#), [11](#), [12](#), [13](#)
7. Dai, A., Nießner, M., Zollhöfer, M., Izadi, S., Theobalt, C.: Bundlefusion: Real-time globally consistent 3d reconstruction using on-the-fly surface reintegration. *ACM Transactions on Graphics (ToG)* **36**(4), 1 (2017) [1](#), [3](#)
8. Deng, T., Shen, G., Qin, T., Wang, J., Zhao, W., Wang, J., Wang, D., Chen, W.: Plgslam: Progressive neural scene representation with local to global bundle adjustment (2023) [3](#)
9. Engel, J., Schöps, T., Cremers, D.: Lsd-slam: Large-scale direct monocular slam. In: European conference on computer vision. pp. 834–849. Springer (2014) [1](#)
10. Huang, J., Huang, S.S., Song, H., Hu, S.M.: Di-fusion: Online implicit 3d reconstruction with deep priors. In: Proceedings of the IEEE/CVF Conference on Computer Vision and Pattern Recognition. pp. 8932–8941 (2021) [1](#), [3](#)
11. Jiang, C., Zhang, H., Liu, P., Yu, Z., Cheng, H., Zhou, B., Shen, S.: H2-mapping: Real-time dense mapping using hierarchical hybrid representation. arXiv preprint arXiv:2306.03207 (2023) [2](#), [5](#)
12. Johari, M.M., Carta, C., Fleuret, F.: Eslam: Efficient dense slam system based on hybrid representation of signed distance fields. In: Proceedings of the IEEE/CVF Conference on Computer Vision and Pattern Recognition. pp. 17408–17419 (2023) [2](#), [3](#), [4](#), [5](#), [6](#), [7](#), [8](#), [9](#), [10](#), [11](#), [12](#), [13](#)
13. Li, J., Zhang, J., Bai, X., Zhou, J., Gu, L.: Efficient region-aware neural radiance fields for high-fidelity talking portrait synthesis. In: Proceedings of the IEEE/CVF International Conference on Computer Vision. pp. 7568–7578 (2023) [2](#), [5](#)
14. Li, Z., Müller, T., Evans, A., Taylor, R.H., Unberath, M., Liu, M.Y., Lin, C.H.: Neuralangelo: High-fidelity neural surface reconstruction. In: Proceedings of the IEEE/CVF Conference on Computer Vision and Pattern Recognition. pp. 8456–8465 (2023) [1](#), [5](#)
15. Ma, Z., Zhu, X., Qi, G.J., Lei, Z., Zhang, L.: Otavatar: One-shot talking face avatar with controllable tri-plane rendering. In: Proceedings of the IEEE/CVF Conference on Computer Vision and Pattern Recognition. pp. 16901–16910 (2023) [2](#), [5](#)
16. Mildenhall, B., Srinivasan, P.P., Tancik, M., Barron, J.T., Ramamoorthi, R., Ng, R.: Nerf: Representing scenes as neural radiance fields for view synthesis. *Communications of the ACM* **65**(1), 99–106 (2021) [1](#), [3](#)
17. Müller, T., Evans, A., Schied, C., Keller, A.: Instant neural graphics primitives with a multiresolution hash encoding. *ACM Transactions on Graphics (ToG)* **41**(4), 1–15 (2022) [2](#), [5](#)

18. Newcombe, R.A., Izadi, S., Hilliges, O., Molyneaux, D., Kim, D., Davison, A.J., Kohi, P., Shotton, J., Hodges, S., Fitzgibbon, A.: Kinectfusion: Real-time dense surface mapping and tracking. In: 2011 10th IEEE international symposium on mixed and augmented reality. pp. 127–136. Ieee (2011) [1](#), [3](#)
19. Newcombe, R.A., Lovegrove, S.J., Davison, A.J.: Dtam: Dense tracking and mapping in real-time. In: 2011 international conference on computer vision. pp. 2320–2327. IEEE (2011) [1](#), [3](#)
20. Nießner, M., Zollhöfer, M., Izadi, S., Stamminger, M.: Real-time 3d reconstruction at scale using voxel hashing. *ACM Transactions on Graphics (ToG)* **32**(6), 1–11 (2013) [1](#), [3](#)
21. Or-El, R., Luo, X., Shan, M., Shechtman, E., Park, J.J., Kemelmacher-Shlizerman, I.: Stylesdf: High-resolution 3d-consistent image and geometry generation. In: Proceedings of the IEEE/CVF Conference on Computer Vision and Pattern Recognition. pp. 13503–13513 (2022) [1](#), [6](#)
22. Schops, T., Sattler, T., Pollefeys, M.: Bad slam: Bundle adjusted direct rgb-d slam. In: Proceedings of the IEEE/CVF Conference on Computer Vision and Pattern Recognition. pp. 134–144 (2019) [1](#), [3](#)
23. Straub, J., Whelan, T., Ma, L., Chen, Y., Wijmans, E., Green, S., Engel, J.J., Mur-Artal, R., Ren, C., Verma, S., et al.: The replica dataset: A digital replica of indoor spaces. *arXiv preprint arXiv:1906.05797* (2019) [8](#), [9](#), [10](#), [12](#), [13](#), [14](#)
24. Sturm, J., Engelhard, N., Endres, F., Burgard, W., Cremers, D.: A benchmark for the evaluation of rgb-d slam systems. In: 2012 IEEE/RSJ international conference on intelligent robots and systems. pp. 573–580. IEEE (2012) [2](#), [8](#), [9](#), [10](#), [12](#)
25. Sucar, E., Liu, S., Ortiz, J., Davison, A.J.: imap: Implicit mapping and positioning in real-time. In: Proceedings of the IEEE/CVF International Conference on Computer Vision. pp. 6229–6238 (2021) [2](#), [3](#), [4](#), [9](#)
26. Teed, Z., Deng, J.: Droid-slam: Deep visual slam for monocular, stereo, and rgb-d cameras. *Advances in neural information processing systems* **34**, 16558–16569 (2021) [1](#), [3](#)
27. Vespa, E., Nikolov, N., Grimm, M., Nardi, L., Kelly, P.H., Leutenegger, S.: Efficient octree-based volumetric slam supporting signed-distance and occupancy mapping. *IEEE Robotics and Automation Letters* **3**(2), 1144–1151 (2018) [1](#)
28. Wang, H., Wang, J., Agapito, L.: Co-slam: Joint coordinate and sparse parametric encodings for neural real-time slam. In: Proceedings of the IEEE/CVF Conference on Computer Vision and Pattern Recognition. pp. 13293–13302 (2023) [2](#), [3](#), [4](#), [5](#), [8](#), [9](#), [10](#), [11](#), [12](#), [13](#)
29. Wang, J., Bleja, T., Agapito, L.: Go-surf: Neural feature grid optimization for fast, high-fidelity rgb-d surface reconstruction. In: 2022 International Conference on 3D Vision (3DV). pp. 433–442. IEEE (2022) [8](#)
30. Wang, P., Liu, L., Liu, Y., Theobalt, C., Komura, T., Wang, W.: Neus: Learning neural implicit surfaces by volume rendering for multi-view reconstruction. *arXiv preprint arXiv:2106.10689* (2021) [1](#)
31. Wang, P., Liu, Y., Chen, Z., Liu, L., Liu, Z., Komura, T., Theobalt, C., Wang, W.: F2-nerf: Fast neural radiance field training with free camera trajectories. In: Proceedings of the IEEE/CVF Conference on Computer Vision and Pattern Recognition. pp. 4150–4159 (2023) [1](#)
32. Whelan, T., Kaess, M., Fallon, M., Johannsson, H., Leonard, J., McDonald, J.: Kintinuous: Spatially extended kinectfusion (2012) [1](#), [3](#)
33. Yang, X., Li, H., Zhai, H., Ming, Y., Liu, Y., Zhang, G.: Vox-fusion: Dense tracking and mapping with voxel-based neural implicit representation. In: 2022 IEEE In-

- ternational Symposium on Mixed and Augmented Reality (ISMAR). pp. 499–507. IEEE (2022) [2](#), [3](#), [4](#), [8](#), [9](#), [11](#), [12](#)
34. Zeng, M., Zhao, F., Zheng, J., Liu, X.: Octree-based fusion for realtime 3d reconstruction. *Graphical Models* **75**(3), 126–136 (2013) [1](#), [3](#)
35. Zhu, Z., Peng, S., Larsson, V., Xu, W., Bao, H., Cui, Z., Oswald, M.R., Pollefeys, M.: Nice-slam: Neural implicit scalable encoding for slam. In: Proceedings of the IEEE/CVF Conference on Computer Vision and Pattern Recognition. pp. 12786–12796 (2022) [2](#), [3](#), [4](#), [8](#), [9](#), [10](#), [11](#), [12](#), [13](#)
36. Zhuang, Y., Zhang, Q., Feng, Y., Zhu, H., Yao, Y., Li, X., Cao, Y.P., Shan, Y., Cao, X.: Anti-aliased neural implicit surfaces with encoding level of detail. In: SIGGRAPH Asia 2023 Conference Papers. pp. 1–10 (2023) [2](#), [5](#)